



A Perspective on the Scaling of Magnetosheath Turbulence and Effects of Bow Shock Properties

Eliza Teodorescu¹ , Marius Echim^{1,2} , and Gabriel Voituca¹ 

¹ Institute of Space Science (ISS), Măgurele, Romania; eliteo@spacescience.ro

² The Royal Belgian Institute for Space Aeronomy (BIRA-IASB), Brussels, Belgium

Received 2020 December 15; revised 2021 January 27; accepted 2021 January 27; published 2021 March 26

Abstract

We analyze magnetic field data from two magnetosheath crossings, representative of a larger collection of similar cases in the database of the Cluster spacecraft. We apply a novel data analysis method to identify the power-law behavior of the structure functions and to find the validity range of the power-law scaling. We validate the technique with solar wind magnetic field data and a synthetic magnetic field signal. This approach grants a rigorous determination of the scale range for a linear fit of the structure function in the log–log representation, which most often is chosen arbitrarily. The fitting allows an estimation of the power spectral index from the scale variation of the second-order structure function exponent. Data recorded during the first Cluster magnetosheath crossing, called *Event 1*, indicate three different power-law scaling regimes (injection, inertial, and kinetic) separated by two spectral breaks, consistent with the scenario of fully developed turbulence. However, data from the second Cluster magnetosheath crossing, called *Event 2*, depict a different scenario with only two power-law scaling regimes determined from the fit. A spectral slope shallower than the Kolmogorovian solar wind power-law index is determined at magnetohydrodynamic scales, spanning more than three frequency decades, which is separated by a spectral break from the kinetic regime. An analysis of simultaneous solar wind data from the Advanced Composition Explorer suggests that the scale behavior of the magnetosheath fluctuations might be controlled by the structure of the bow shock; solar wind turbulent fluctuations are only partially destroyed while they are carried across the bow shock. Both events are recorded in a quasi-perpendicular magnetosheath.

Unified Astronomy Thesaurus concepts: [Interplanetary turbulence \(830\)](#); [Solar-terrestrial interactions \(1473\)](#); [Planetary bow shocks \(1246\)](#); [Interplanetary magnetic fields \(824\)](#); [Space plasmas \(1544\)](#)

1. Introduction

Heliospheric plasmas such as the solar wind or the planetary magnetosheaths are naturally found in a turbulent state. Turbulence is discussed both in terms of wave superposition, questioned by Matthaeus & Goldstein (1982), Bruno et al. (1985), Roberts et al. (1987a, 1987b), Grappin et al. (1989), Grappin et al. (1990), Tu et al. (1989), or Marsch & Tu (1990), or as arising from the interaction of coherent structures (Tu & Marsch 1995). More recently, efforts have been made to reconcile the two approaches describing plasmaturbulence: waves versus coherent structures interaction. Newell et al. (2001), Roberts et al. (2013), Lesur et al. (2014a, 2014b), Valentini et al. (2014), Pucci et al. (2018), Grošelj et al. (2019), Roberts et al. (2020b), and Chang (2015) addressed the subject of complexity in space plasmas. Fundamental aspects of the turbulent dynamics of astrophysical plasma are discussed predominantly based on solar wind observations (Tu & Marsch 1995; Goldstein et al. 1995; Bruno & Carbone 2013; Alexandrova et al. 2013).

A characteristic power-law scaling of the power spectral density (PSD) is typically interpreted as the trademark of turbulence. The possible universal scaling behavior of small-scale fluctuations observed in fully developed turbulence involves power-law scaling for all moments of fluctuations, i.e., structure functions (SF, Frisch 1995), at inertial-range scales, where energy transfer dominates energy injection or dissipation. We recall the standard definition of the structure function:

$$SF_q = \langle |\delta X(\tau)|^q \rangle = \int_{-\delta X_{\max}}^{+\delta X_{\max}} |\delta X(\tau)|^q P(\delta X, \tau) d\delta X. \quad (1)$$

Kolmogorov (1962, 1941) hypothesized that the power-law exponents of the velocity differences across a distance l , ζ_q , and

the average energy dissipated over a ball of size l , τ_q , are related for positive moment orders q through $\zeta_q = q/3 + \tau_{q/3}$. Energy dissipation is independent of scale, $t_q = 0$, consequently,

$$\zeta_q = q/3. \quad (2)$$

For the averaged kinetic energy, i.e., second-order SF of the velocity fluctuations ($q = 2$), Equation (2) leads to the well-known $2/3$ law (e.g. She & Leveque 1994). This scaling has been determined both experimentally and numerically (Stolovitzky et al. 1992; Thoroddsen & Van Atta 1992; Chen et al. 1993).

Other works (e.g., Anselmet et al. 1984; Vincent & Meneguzzi 1991) have shown that for moment orders larger than 3, there are large deviations of the scaling exponent from $q/3$. The phenomenon responsible for these deviations is referred to as intermittency, and significant efforts have been invested in the development of phenomenological models in order to account for the nonlinear scaling of the SF (see, e.g., Bruno 2019, for a review). For example, Horbury & Balogh (1997) compared four intermittency models: the β model (Frisch et al. 1978), the random β model (Paladin & Vulpiani 1987), the p -model (Meneveau & Sreenivasan 1987a, 1987b), and the She & Leveque (1994) model with heliospheric turbulence observations (Burlaga 1991; Carbone 1994; Grauer et al. 1994; Ruzmaikin et al. 1995; Horbury et al. 1996). For polar heliosphere, Horbury & Balogh (1997) find that the fluctuations are best described by the p -model, but also point out the remarkable predictions of the She and Leveque 2D variant. Using fast-latitude scan of Ulysses, Pagel & Balogh (2001) showed that for magnetic field fluctuations and at inertial-range frequencies, the structure function analysis with respect to the time lag fits the data better than the extended self-similarity analysis

(Benzi et al. 1993), which involves plotting against the third-order structure function. They also showed that the Kolmogorov picture of turbulence better describes the solar wind than the Kraichnan (1965) theory.

Many authors have discussed the need for higher-order statistics in the analysis of turbulence, particularly when intermittency is present and second-order statistics such as Fourier analysis are insufficient (see, e.g., Monin & Yaglom 1975; Dudok de Wit & Krasnoselskikh 1996). Pagel & Balogh (2001) stressed that higher-order moments are required to describe the scaling of fluctuations characterized by non-Gaussian probability distributions and pointed out that the scaling determined by Kolmogorov (1941, 1962) for the power spectrum ($-5/3$) or the second-order structure function ($2/3$) in ideal fluid flows in general also characterize intermittent systems as the corrections are very small for low orders of the structure function. The SF analysis is an extensively used method, also applied in neutral turbulence studies, that is able to link the observed statistics to the underlying dynamics of fluctuations and provide straightforward means to discriminate between various theoretical models (Horbury & Balogh 1997; Pulkkinen et al. 2006). Using wall pressure measurements performed in a transsonic wind tunnel, Schulz-DuBois & Rehberg (1981) demonstrated that SF can be more accurately computed with one to two orders fewer data than the correlation function (i.e., the power spectra). On the other hand, Ruzmaikin et al. (1995) reported that the observed spectral scaling of non-Gaussian processes is composed of a spectral exponent and an intermittency exponent and cannot be directly compared to Kolmogorov (1941) and Iroshnikov (1964)-Kraichnan (1965) standard spectral theories. Huang et al. (2010) argued that scaling exponents determined from second-order SF are influenced by large energetic scales ($f < 1$ Hz) and that a shorter inertial range is predicted by this approach. We note that our method involves several-order moments for the estimation of the power-law exponents and the boundaries of the scale ranges that are characteristic to the turbulent fluctuations measured in the bounded environment of the Earth's magnetosheath that is analyzed in this paper.

Earth's magnetosheath is a trademark environment for complex and nonlinear interactions (Schwartz et al. 1996, for a review) that forms between two boundaries, the magnetopause and the bow shock, i.e., a shock wave resulting in the interaction of the solar wind with Earth's magnetosphere that slows down the supersonic and super-Alfvénic solar wind plasma (Dudok de Wit & Krasnoselskikh 1996). Mass, momentum, and energy conservation together with collisionless dissipation processes across and near the bow shock determine the properties of the magnetosheath. Two regimes are defined with respect to the angle between the interplanetary magnetic field (IMF) and the shock normal: quasi-parallel and quasi-perpendicular geometries, corresponding to angles lower or higher than 45° , respectively. It has been demonstrated that turbulence properties in the magnetosheath are strongly dependent on the bow-shock angle (Shevyrev et al. 2006) and that considerably different shock dissipation processes characterize the two magnetosheath regions (Omidi et al. 2005, reviews by Tsurutani & Stone 1985). Dissipation in quasi-perpendicular shocks relates to ion cyclotron waves (propagating in the direction parallel to the magnetic field) and mirror-mode waves that are carried by the magnetosheath flow. Lessons learned from solar wind turbulence (e.g., Bale et al. 2009;

Telloni et al. 2019; Telloni 2021) indicate the strong correlation of these waves with plasma beta and temperature anisotropy. In quasi-parallel geometry, ion beam populations (formed due to reflection and leakage at the shock) interact with the solar wind and produce waves and nonlinear structures that have a significant impact on the magnetosheath, comparable with the effect of fore-shock bubbles or hot-flow anomalies resulting from the interaction between solar wind discontinuities and the bow shock (Russell & Farris 1995; Czaykowska et al. 2001; Omidi et al. 2014). The role of turbulence-generated structures at proton scales in the magnetosheath is discussed by Voros et al. (2016).

The turbulence properties in the quasi-parallel and quasi-perpendicular magnetosheath have similarities but also significant differences for a large range of scales, from magnetohydrodynamic (MHD) to electron scales. Some observations reveal the $f^{-5/3}$ power law in quasi-parallel magnetosheath at MHD scales (similar to the inertial range observed in the solar wind), indicative of developed turbulence. In quasi-perpendicular geometry, no such spectrum is observed (Shevyrev et al. 2006; Breuillard et al. 2018). Other studies (Alexandrova et al. 2008; Huang et al. 2017; Teodorescu & Echim 2020) show that an inertial range exists in the magnetosheath flanks and closer to the magnetopause. Steeper slopes of magnetosheath turbulence are reported closer to the magnetopause for the inertial scales (Sahraoui et al. 2006) and shallower, f^{-1} , near the bow shock (Czaykowska et al. 2001; Dwivedi et al. 2019).

In the kinetic regime of scales, a wide range of scaling indices is reported (e.g., Smith et al. 2006). More recently, magnetic and density observations (e.g., Alexandrova et al. 2009, 2012; Sahraoui et al. 2009; Chen et al. 2010, 2012, 2013; Salem et al. 2012; Roberts et al. 2020a) have shown that an $f^{-8/3}$ spectrum is more common at these scales. Kinetic simulations at sub-ion scales (Howes et al. 2011) show that Landau damping can explain this steepening, while Boldyrev & Perez (2012) derived such an index when considering 2D intermittent structure. This model describes the kinetic scale behavior observed either in the solar wind (Alexandrova et al. 2009; Kiyani et al. 2009; Chen et al. 2010, 2012, 2013; Sahraoui et al. 2013) or in the magnetosheath (Chen & Boldyrev 2017) in the first decade of sub-ion scales. Chen & Boldyrev (2017) also propose a new type of turbulence, inertial kinetic Alfvén, to account for the even steeper slopes, i.e., $-11/3$, of the magnetosheath magnetic fluctuations, computed closer to the electron scales. Much steeper scaling has been found for sub-electron scales (see e.g., Huang et al. 2014 and references therein). Spectral indices steeper than -3 , generally typical of sub-ion scales, are not reliably determined based on fluctuations computed from two-point SF (Monin & Yaglom 1975) due to leakage from large scales. Chen et al. (2010) observe the anisotropy of fast solar wind turbulence using this method and point out its limitations. Examining the scaling of magnetosheath fluctuations in the sub-ion regime, Wang et al. (2020) determine that spectral indices computed from two-point second-order SF are flatter than those computed from three- and five-point second-order SF (which agree with each other). These methodologies would be interesting to explore in a future analysis.

It is generally accepted that turbulent fluctuations formed in the solar wind or at the bow shock penetrate a quasi-parallel magnetosheath, while in the quasi-perpendicular case, fluctuations are mainly created locally and the energy is transferred

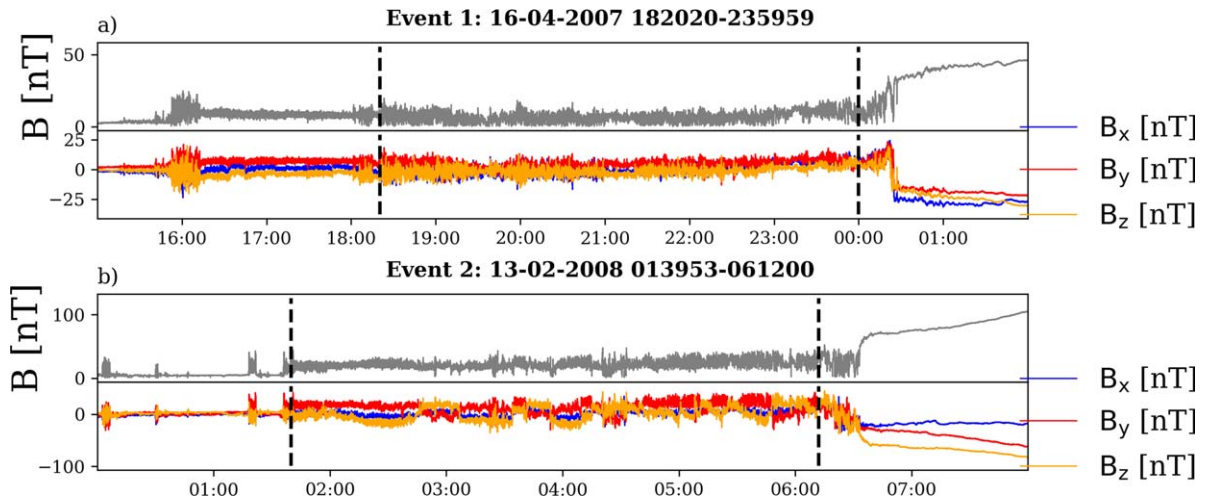


Figure 1. Time series of the total magnetic field (solid gray line) and the magnetic field components B_x , B_y , and B_z in GSE coordinates (solid blue, red, and orange lines) recorded by Cluster 3 in the time intervals (a) 2007 April 16, 15:00–April 17, 02:00 and (b) 2008 February 12, 00:00–February 13, 08:00. The vertical dashed black lines identify the data intervals treated in this study, *Event 1* and *Event 2*.

Table 1
Magnetic Field and Plasma Conditions in the Magnetosheath of the Two Selected Events

Event/Average Values	Magnetosheath							
	B (nT)	N (cm^{-3})	v (km s^{-1})	T (K)	v_A (km s^{-1})	beta	q_{Bn}	a_{Bv}
Event 1 16.04.2007	7.	16.	198.	72.	9.7	9.3	90	90
Event 2 13.02.2008	22.	11.	243.	464.	77.9	4.3	80	100

from injection scales directly to kinetic scales. As a consequence, an inertial range is found in the magnetosheath behind a quasi-parallel shock or in the flanks, far away from the bow shock, where fluctuations have had enough time to evolve into a more developed turbulence.

In this paper we report on the properties of turbulent fluctuations of the magnetic field at scales characteristic to what is typically considered the inertial range measured in quasi-perpendicular magnetosheath configuration during two events recorded at solar minimum by the Cluster spacecraft (Escoubet et al. 1997). The state of the upstream solar wind is determined from data provided by the Advanced Composition Explorer (ACE; Stone et al. 1998). The magnetosheath geometry for the two events is estimated based on a model proposed by Farris et al. (1991) and Farris & Russell (1994), as explained below. We determine the scaling properties of magnetic field fluctuations with a novel rank-ordering technique based on SF computation (Tam & Chang 2011) to identify power-law regimes and the corresponding scaling range. We validate the technique with in situ solar wind data provided by ACE and with synthetic data with prescribed properties, and we confirm the results through spectral analysis.

2. Cluster Magnetosheath Data. Estimation of the Bow-shock Geometry

We analyze magnetic field records from the Cluster Fluxgate Magnetometer—FGM (Balogh et al. 1997) for two magnetosheath traversals, called *Event 1*, recorded in 2007 April 16, 18:20:20–23:59:59, and *Event 2*, recorded in 2008 February 13, 01:39:53–06:12:00. The time series of the components and the total magnetic field measured during the two events are represented in Figure 1. The magnetic field data are provided at

a time resolution of 22 Hz. A large collection of carefully selected Cluster magnetosheath traversals is available at <http://www.storm-fp7.eu> for the solar maximum in 2001–2002 and for the solar minimum in 2007–2008.

The plasma moments (density, bulk velocity, etc.) are provided by the Cluster Ion Spectrometry—Hot Ion Analyzer, CIS-HIA (Rème et al. 1997) with a resolution of 4 s. The average values of the main physical parameters (magnetic field, plasma density, plasma velocity and Alfvén speed, plasma beta, and the angle between the magnetic and the plasma velocity— θ_{Bv}) observed for the two events are summarized in Table 1. We also investigate the state of the solar wind at the time of the two Cluster events from measurements provided by ACE. We extrapolate the state of the solar wind in the vicinity of Earth’s bow shock and apply the flat time-delay method (Mailyan et al. 2008; Munteanu et al. 2013) to account for the time delay between the moment of the actual ACE measurements and the moment of impact at the Earth’s bow shock.

2.1. Magnetosheath Data Selection

The two magnetosheath traversals analyzed in this study are recorded under relatively quiet conditions (stationary and slowly fluctuating fields), but the upstream solar wind conditions differ between the two events, as summarized in Tables 1 and 2. The solar wind has an average velocity of $\sim 310 \text{ km s}^{-1}$ and 630 km s^{-1} during *Event 1* and *Event 2*, respectively. The IMF fluctuates around 3 and 5 nT for the two events, respectively, with a plasma density of $\sim 3 \text{ particles/cm}^{-3}$ and hotter plasma in the fast solar wind. Table 1 indicates that for different upstream bow-shock conditions, we find similar magnetosheath plasma bulk velocities for the two events, denser plasma under slow solar

Table 2
Magnetic Field and Plasma Conditions in the Solar Wind Before and During the Two Magnetosheath Traversals Described in Table 1

Event/Average Values	Solar Wind							
	B (nT)	σ_B	N (cm $^{-3}$)	σ_N	v (km s $^{-1}$)	σ_v	T (eV)	σ_T
Event 116.04.2007	2.38	0.48	2.62	0.73	307	4.04	1.54	0.32
Event 213.02.2008	4.7	0.46	3.25	0.27	629	13.72	14.3	1.9

wind conditions (*Event 1*), and a higher magnetic field for fast solar wind conditions (*Event 2*).

We assume that the Taylor hypothesis (Taylor 1938) is satisfied in the magnetosheath; indeed, the plasma bulk velocity, $v_{\text{flow}} \sim 200 \text{ km s}^{-1}$, is much greater than the Alfvén speed (v_A) for both selected events, $v_A = 9.7 \text{ km s}^{-1}$ and $v_A = 77.9 \text{ km s}^{-1}$, respectively (also summarized in Table 1). Thus we assume that the timescales, τ , and the spatial scales, L , are linked by $L = v_{\text{flow}}\tau$ (see e.g., Sundkvist et al. 2007). We note that $v_{\text{flow}}/v_A \sim 3$ for *Event 2*. Klein et al. (2014) suggest that a ratio of $v_{\text{flow}}/v_A \leq 3$ significantly flattens the spectrum at frequencies higher than the ion gyrofrequency. Due to limited measurement resolution (22 Hz), we can only partially access the sub-ion regime, therefore a rigorous analysis at these frequencies is not possible. Another feature that supports the validity of Taylor’s hypothesis is that for both events, the magnetosheath magnetic field is mostly perpendicular to the mean flow direction with an angle between the magnetic field and the plasma bulk velocity, α_{Bv} , of about 90° for *Event 1* and about 105° for *Event 2*. A 2.5D simulation by Perri et al. (2017) demonstrates that in such cases, Taylor’s hypothesis remains valid for flow speeds typical of magnetosheath ($5v_A$) and solar wind ($20v_A$).

3. Determination of the Bow-shock Geometry

An extensive study by Tátrallyay et al. (2012) compares several magnetopause models (Shue et al. 1998; Lin et al. 2010) proposed a new model based on Verigin et al. (2009) as well as bow-shock models (Farris et al. 1991, combined with Farris & Russell 1994; Cairns et al. 1995, combined with Farris & Russell 1994; Jerab et al. 2005; Verigin et al. 2001b, 2001a, 2003). They suggest that the magnetopause position is best predicted by Lin et al. (2010), and that the model of Farris et al. (1991) and Farris & Russell (1994) estimates the position of the bow shock best compared to in situ observations by Cluster.

In our study we determine the bow-shock geometry using ACE magnetic field solar wind data (Smith et al. 1998) mapped at the Earth’s bow shock. The position and shape of the shock is estimated from the empirical two-dimensional model proposed by Farris et al. (1991)

$$R_{BS} = R_{BS_0} \frac{1 + \epsilon}{1 + \epsilon \cos \theta}, \quad (3)$$

where R_{BS} is the bow-shock (BS) radial distance, θ is the solar zenith angle in aberrated coordinates, $\epsilon = 0.81$ is the eccentricity estimated by Farris et al. (1991), and R_{BS_0} is the bow-shock standoff distance computed from in situ ACE measurements as proposed by Farris & Russell (1994) as

$$R_{BS_0} = R_{MP_0} \left(1 + 1.1 \frac{(\gamma - 1)M_{ms}^2 + 2}{(\gamma + 1)M_{ms}^2 - 1} \right), \quad (4)$$

where $M_{ms} = V_{sw}/V_{ms}$ is the magnetosonic Mach number, $\gamma = 5/3$ is the polytropic index, and R_{MP_0} , the magnetopause

position, is fixed at $10.5 R_E$ (Lin et al. 2010). The BS profiles determined from Equations (3) and (4) fit the observations by Cluster well, as illustrated in Figure 2.

To determine the shock geometry for a Cluster magnetosheath traversal, we project satellite observations on the model bow shock and assume that the spacecraft is connected to the bow shock by straight magnetic field lines (see, e.g., Eastwood et al. 2005). The time intervals analyzed in this work span several hours, during which Cluster moves more than 4 Earth radii through the magnetosheath. Figure 2 (b), lower left and right panels, illustrate Cluster orbits for *Event 1* and *Event 2*, respectively (orange lines). This study is part of a larger statistical analysis targeting the entire database of Cluster magnetosheath traversals. The model magnetosheath (i.e., the region between the model magnetopause and the model bow shock) is divided into sectors, as sketched in Figure 2 (b) (see the dotted gray lines). We determine the sector in which the Cluster orbit is located and compute the normal to the bow shock at the left edge of this sector (see Figure 2). This is the reference value of the bow-shock normal assumed for the respective Cluster orbit.

We then compute θ_{Bn} , the angle between the shock normal and each of the magnetic field vectors collected in the solar wind by ACE. Thus, we obtain the variation of θ_{Bn} with time, as shown in Figure 2 (a); the solar wind magnetic field is overimposed in red. We consider that the shock geometry is quasi-parallel when θ_{Bn} is smaller than 45° and quasi-perpendicular when θ_{Bn} is higher than 45° (Balogh et al. (2005)). A magnetosheath traversal is considered to pertain to one of the two categories or geometries, quasi-parallel or quasi-perpendicular, when at least 85% of the values calculated for θ_{Bn} are lower or higher than 45° , respectively. The two events considered in this study largely satisfy the conditions for a quasi-perpendicular geometry, i.e., θ_{Bn} systematically takes values higher than 45° , as illustrated in Figure 2. The geometry of the bow shock was verified from in situ Cluster data during crossings of the shock for the two events and confirms the findings of the method outlined above.

4. An Automatic Multi-order Power-law-fitting Algorithm (AMPA) to Estimate Scale Invariance

We investigate the scaling properties of magnetic field fluctuations observed in the extreme plasma environment of the quasi-perpendicular turbulent magnetosheath of Earth. We conduct an analysis based on SF computation. The scaling indices are computed for frequency ranges above and below the proton gyrofrequency, thus for scales pertaining to the inertial and kinetic regimes, respectively.

We analyze Cluster data from two traversals of the magnetosheath recorded under slow and fast upstream solar wind conditions, respectively. θ_{Bn} takes values of about 90° for *Event 1* and about 80° for *Event 2*. Thus, both traversals correspond to a quasi-perpendicular geometry.

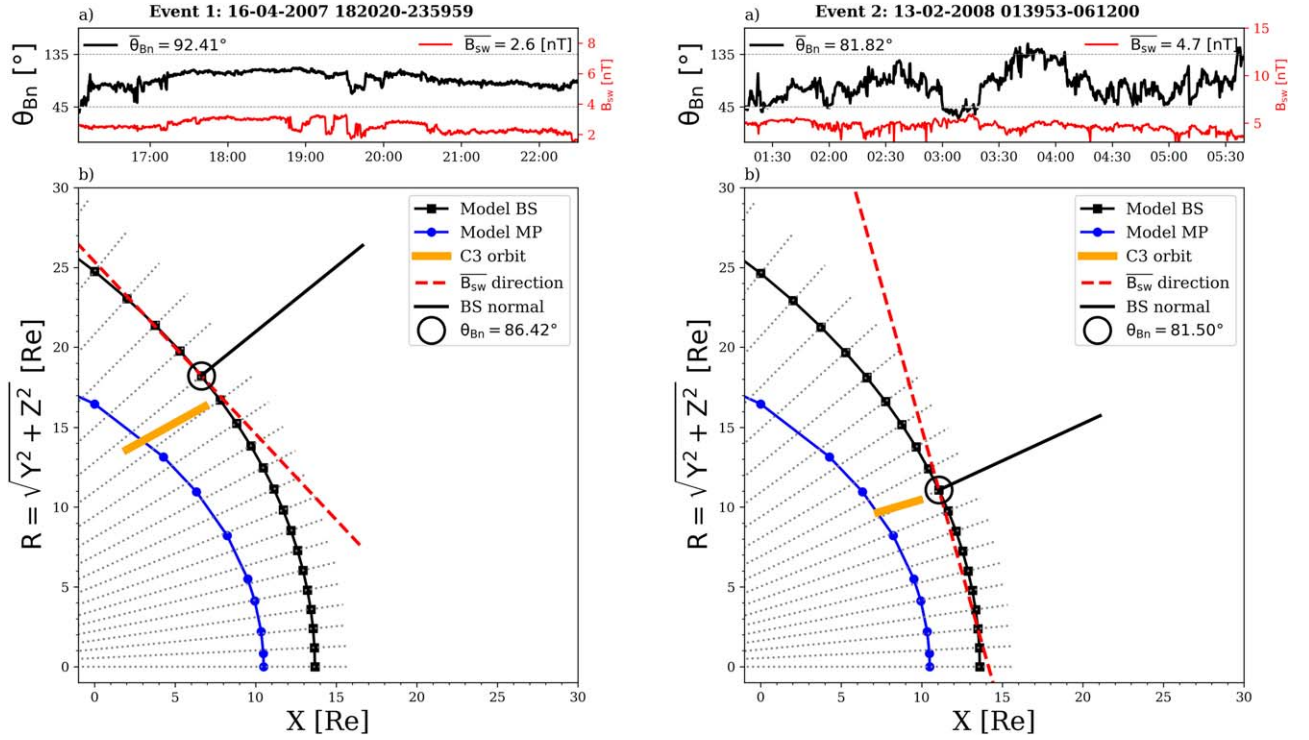


Figure 2. Upper panels (a): time evolution of the angle between the solar wind magnetic field and the normal to the bow shock, θ_{Bn} (solid black line), computed from ACE measurements of the IMF (red solid line). Lower panels (b): model magnetopause (MP—blue curve) and bow shock (BS—black curve), Cluster-3 traversal of the magnetosheath (solid orange line) and the angle between the shock normal (solid black line) and the mean solar wind magnetic field orientation (dashed red line). Left and right panels correspond to *Event 1* and *Event 2*.

Generally, structure function scaling is estimated from a linear fit in the log–log representation over a range of scales, ΔL_a . However, the limits of the fitting interval, ΔL_a , are often arbitrary, such that the linear fit may extend over regions where the variation of the structure function with scale is nonlinear in log–log. Here we derive a method that identifies the existence of a power-law scaling and finds the range of scales where this scaling is valid. The idea stems from the technique used by Tam & Chang (2011) for a rank-ordered multifractal analysis of the auroral electric field.

Our algorithm identifies automatically the limits of the range of scales, δL_s , where the structure function shows a power-law scaling, $SF_q^{-\zeta}$. The algorithm also provides the value of ζ . The mathematical kernel of this approach is based on a statistical analysis of SF adapted from a technique originally developed by Tam & Chang (2011) for the rank-ordered multifractal analysis. We call this procedure the automatic multi-order power-law-fitting algorithm (AMPA) and describe it in detail below.

The range of (time) scales that belong to a power-law regime characterized by the same scaling index is found by evaluating the accuracy of a linear regression of the structure function values within that range. It is assumed that the power-law regimes characterized by different scaling indices are contiguous and that the change in scaling between two adjacent regimes is abrupt (Tam & Chang 2011).

The technique proceeds as follows. A first set of minimum three timescales, starting from the smallest ones, is selected and a linear fit is applied on the corresponding SF in the log–log representation. The goodness of fit is evaluated through a measure called discrepancy, δy , that takes into account how far the considered points are spread out from the straight line

according to

$$(\delta y)_{N,q} = \sqrt{\frac{1}{n_N} \sum_j [y_{j,q} - (a_{N,q}x_j + b_{N,q})]^2} \quad (5)$$

(Equation (12) in Tam & Chang 2011), where n_N is the number of SF fitted points, $j = 1, \dots, n_N$, $y_q = (a_{N,q}x + b_{N,q})$ is the equation of the fitted line, $x = \log \tau$, $y_q = \log SF_q(\tau)$.

The discrepancy δy is computed for structure function values computed for all moment orders, q . A global measure of the overall convergence is given by the root-mean-square discrepancy over all the moment orders,

$$(\Delta y)_N = \sqrt{\langle (\delta y)_{N,q}^2 \rangle_q}. \quad (6)$$

According to Tam & Chang (2011), Δy is a good approximation of the average fractional deviation of the structure function from the fitted line,

$$\left(\frac{\Delta S}{S}\right) \Big|_N = (\ln(10)) \Delta y_N. \quad (7)$$

A set of three consecutive timescales, $\{f_1, f_2, f_3\}$, is considered as pertaining to the same power-law regime if

$$(\Delta S/S) \Big|_N \leq 0.1, \quad (8)$$

which implies an average deviation of 10% or less of the structure function values from the respective fitted lines in the log–log plots. An important merit of the method, see Equation (6), is that it searches for a global convergence in the sense of a power-law scaling for a range of moment orders, (q_1, \dots, q_{\max}) , of SF, where q_{\max} is the maximum order for which the corresponding structure function still provides meaningful results and can be computed

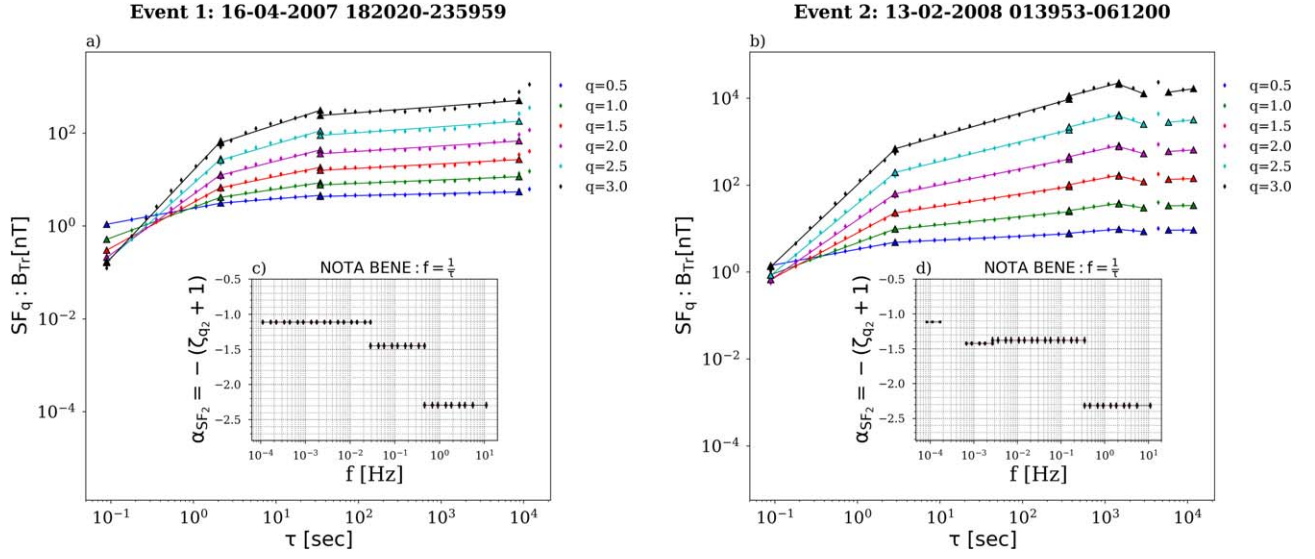


Figure 3. Log–log representation of SF_q vs. timescale, τ , (solid diamonds) computed with AMPA for the magnetic field measured in the Earth’s magnetosheath. The solid lines represent the fitted straight lines to the SF_q , and solid triangles indicate the boundary between two adjacent scale regimes. The SF_q correspond to the trace of the magnetic field. (a) *Event 1* (2007 April 16, 18:20:20–23:59:59), and (b) *Event 2* (2008 February 13, 01:39:53–06:12:00). The inset plots (c) and (d) show the 2D representation of SF_2 scaling indices for the determined scale regimes as a function of frequency $f = 1/\tau$.

from a reasonable number of samples. The maximum relevant moment, q_{\max} , that can be computed for a finite-sized time series can be estimated in various ways, based on statistical reasoning (e.g., Dudok de Wit 2004; Dudok de Wit et al. 2013). We discuss our strategy of determining q_{\max} for the two analyzed events in Section 4.1 and find that $q_{\max} = 3$ in both cases. If the condition is not satisfied, the algorithm moves forward one point and recomputes the discrepancy, Equation (8), for the structure function values pertaining to the new set of three consecutive timescales (this includes two old values, f_2, f_3 , plus a new one, f_4). If the requirement is satisfied for this range, an additional scale, f_5 , is considered for fitting and the measure in Equation (7) is recomputed with a weighing factor given by the number of timescales in the considered subset, $\{f_2, f_3, f_4, f_5\}$.

For subsets larger than three points, a new timescale is added to a power-law regime if $(\Delta S/S)|_N \leq 0.05$ which implies an average uncertainty of the fit of 5% or less. If this requirement is not satisfied, the last timescale in the subset is considered a breaking point and the algorithm restarts from this timescale in search of the following power-law regime, characterized by a different power-law exponent. Thus, the upper limit of a power-law regime characterized by a set of scaling indices $\{\zeta_q^{(a)}\}$ becomes the lower limit for the following adjacent regime characterized by another set of scaling indices $\{\zeta_q^{(b)}\}$. The boundary between two adjacent power-law regimes pertains to both regimes (see also Tam & Chang 2011). We consider that this method ensures an accurate estimation of the power-law scaling regime based on a global convergence of the SF for all moments. Thus, the arbitrariness in evaluating the scaling exponents is much more reduced. In the following, we refer to power-law regimes determined with AMPA, but we discuss the results in terms of scaling indices corresponding to the second-order SF.

The steps described above allow for an identification of the range of scales, ΔL_a , over which the structure function scaling is characterized by the scaling indices $\{\zeta_q^{(a)}\}$. To each scale included in ΔL_a we assign the corresponding structure function

index, $\zeta_q^{(a)}$. The ranges of scales, ΔL , determined from AMPA for *Event 1* and *Event 2* are shown in Figures 3(a) and (b), respectively. The spectral indices corresponding to the second-order SF (SF_2) are depicted for the two events in the inset plots (c) and (d) in Figure 3 as a function of the frequency, f , computed as the inverse of the timescale, τ . The scaling index of SF_2 , $\zeta_2^{(a)}$, has a particular significance. In fully developed turbulence, ζ_2 is related to the spectral index, α , through the relation $\alpha = -\zeta_2 - 1$, (Kolmogorov 1962, 1941). Based on this relation, we then assign a spectral index to each scale included in ΔL_a . The procedure sweeps the full domain of available scales (the lower limit is defined by the measurement resolution, the higher limit is given by the total length of the analysis interval) and find contiguous power-law scaling regimes, $\Delta L_a, \Delta L_b, \dots, \Delta L_p$ that satisfy Equation (8). Thus, in the end we obtain an estimate of the spectral index α for each scale (see the examples in Figures 3 and 4). This procedure has an advantage compared to the classical linear fit of the power spectrum. Indeed, with the AMPA approach, the spectral index is estimated from local scaling properties of the signal for each scale and not from a fit over an arbitrarily chosen range of scales. Also, the scaling range is checked based on the multi-order approach that ensures linearity of SF versus scale globally for all moment orders.

Note also that the links between the scaling of the structure function and the spectral index are explored in a context more general than the Kolmogorovian approach (e.g., Lohse & Müller-Groeling 1995, 1996; Huang et al. 2010).

5. Two Prototypical Examples of Scale Invariance from Cluster Data Downstream the Terrestrial Quasi-perpendicular Shock

Our main effort is devoted to find turbulence scaling laws from magnetic field observations in the Earth’s magnetosheath downstream a quasi-perpendicular shock. As mentioned above, we mainly focus on the results obtained for the second-order SF and its possible links with the spectral index.

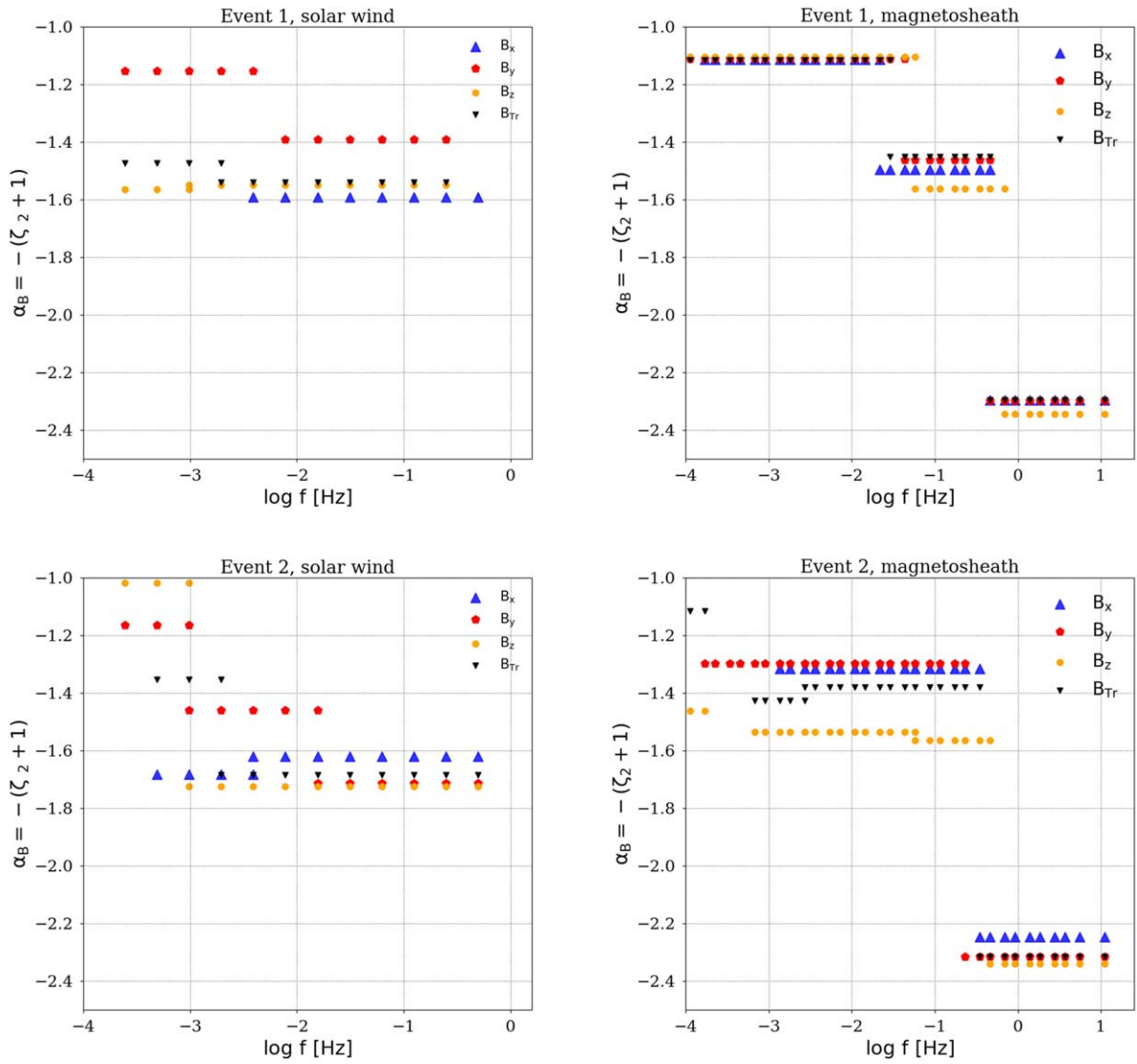


Figure 4. Two-dimensional representation of the scaling indices of solar wind (left panels) and magnetosheath (right panels) magnetic fluctuations computed with AMPA. The computations consider SF for moment orders up to $q = 3$. Data points with the same scaling index, α_B , indicate the scales and frequencies that have been identified by AMPA to pertain to a common regime. The upper panels refer to magnetic field data from ACE (left) and Cluster (right) for *Event 1* (2007 April 16, 18:20:20–23:59:59), and the bottom panels refer to *Event 2* (2008 February 13, 01:39:53–06:12:00). The ACE data are mapped to the bow shock.

AMPA was applied on the three components of the magnetic field, B , and on the trace of B measured during the two Cluster-3 magnetosheath traversals depicted in Figure 1. Figure 4 illustrates the main results and includes the 2D representation of the SF scaling indices determined for different scale/frequency regimes versus spacecraft frequency for magnetic fluctuations measured in the solar wind (left panels) and magnetosheath (right panels). One dot in the graph corresponds to the scaling index estimated with AMPA. Thus, scales pertaining to the same power-law regime (i.e., exhibiting the same order-dependent scaling index) are identified in the 2D representations as collections of points with the same value on the Y -axis, which is precisely the characteristic power-law index, α_B , for the respective scaling regime.

5.1. Scaling of Magnetosheath Turbulence from Structure Function Analysis with AMPA

A rough approximation of the maximum order, q_{\max} , still providing meaningful SF results from finite-sized data samples

can be evaluated as $q_{\max} = \log N - 1$ (Dudok de Wit et al. 2013), where N is the total number of data samples. The data analyzed in this work comprise N samples of about 10^5 , thus q_{\max} would be equal to 4. A more robust technique for determining q_{\max} is proposed by Dudok de Wit (2004) and targets the convergence of the integrand in Equation (4). We evaluate the scale dependent q_{\max} for each magnetic field component based on this latter method. The results (not shown) indicate that for timescales shorter than approximately 30 s (corresponding to roughly 6600 km, assuming Taylor hypothesis), the maximum reliable SF order, q_{\max} , varies between 3 and 5 for all three magnetic field components and both events. As expected, at higher scales, q_{\max} increases as the fluctuations become more Gaussian. For consistency, we use the most conservative value $q_{\max} = 3$ for both events but also compute intermediate orders for better statistics of the AMPA fit. Kiyani et al. (2006) stress that for finite-size samples the conditioning of the data is mandatory, more so as higher-order moments describe the tails of the distribution. As our analysis involves quite low moment-orders ($q_{\max} = 3$), and coupled with the fact

that the probability distributions functions (PDFs, not shown) of the two events do not indicate unexpected extremal values, we do not apply any strategy of data conditioning.

The magnetosheath data analyzed in this study show some specific characteristics to be compared to the general expectation. Indeed, first we note that both events are recorded downstream a quasi-perpendicular shock geometry in the dawn flank of the magnetosheath. Usually, the quasi-perpendicular configuration is associated with the dusk side of the magnetosheath. Also, the magnetic field data are measured starting from the close vicinity of the bow shock, as shown in Figure 2, where we illustrate the relative position of the Cluster spacecraft with respect to the bow-shock and magnetopause models (Farris et al. 1991 and Farris & Russell 1994 and Lin et al. 2010, respectively). The scaling of the structure function was determined by applying the multi-order AMPA algorithm, described above, which identifies the range of scales where the structure function can indeed be fitted by a line in log-log for all considered moment orders.

During *Event 1*, the solar wind is slow, the speed is below 400 km s^{-1} , and the electron temperature is rather low, about 1.5 eV . The shock geometry is estimated based on the bow-shock model by Farris et al. (1991) and Farris & Russell (1994) and using ACE data. It indicates a quasi-perpendicular configuration. The analysis of Cluster data in the magnetosheath shows that at the largest scales, between 10^{-4} and 10^{-2} Hz , the magnetic fluctuations exhibit a global power-law scaling over all SF moments (q from 1 to 3) and all magnetic field components (including the trace of B). In particular, ζ_2 is close to 0 in this range of scales, as indicated in Figure 3(c). This scaling might well correspond to what is traditionally called the injection range. Indeed, if we extrapolate the link between ζ_2 and α , we would obtain a power spectrum scaling index, α , close to -1 .

At intermediate scales, between 0.01 and 0.5 Hz , we found a Kolmogorov-like scaling index with ζ_2 close to $2/3$ (α close to $-5/3$). Interestingly, similar values of the scaling index were reported for quasi-parallel geometry (Shevyrev et al. 2006; Breuillard et al. 2018). At sub-ion scales, between 0.5 and 1 Hz , we find a scaling index ζ_2 close to $3/2$ and a spectral slope close to -2.3 . Modern approaches predict steeper power spectrum slopes for the sub-ion regime (Boldyrev & Perez 2012; Chen & Boldyrev 2017), but the resolution of Cluster fluxgate data used in this study does not allow for the analysis of such smaller scales.

We also note an interesting feature related to solar wind scaling determined with AMPA, albeit for rather short time intervals as delimited by the magnetosheath analysis. While the fast wind example (associated with *Event 2*) shows a scaling index close to -1 at lower frequencies, the slow wind event does not exhibit such a scaling. This difference may be due to saturation of fluctuations at the larger scales in the slow solar wind, as discussed by Bruno et al. (2019).

In summary, the picture emerging from the analysis of magnetosheath turbulence during *Event 1* and based on structure function scaling is that of three different power-law scaling regimes and two breaks. Indeed, we found (i) an extended range at large scales in which the fluctuations of all magnetic components are uncorrelated, characterized by ζ_2 close to 0, (ii) a rather narrow range of scales where the scaling index, ζ_2 , is close to $2/3$, typical for what is generally called the inertial range, and (iii) a third scaling regime consistent with

higher values of ζ_2 . Except for the narrowness of the intermediate (inertial) range, this picture seems to be consistent with the scenario of fully developed turbulence and bears similarities with results reported for turbulence scaling downstream a quasi-parallel shock.

The Cluster data during *Event 2* correspond to different upstream conditions. Indeed, the solar wind is fast, the speed takes values of about 600 km s^{-1} , and the electron temperature is about 15 eV . The geometry of the shock is quasi-perpendicular. Interestingly, the background conditions in the magnetosheath are significantly different between the two events. The Cluster data recorded during *Event 2* show that the magnetosheath plasma is less dense, the plasma beta is smaller, and the magnetic field intensity is higher than for *Event 1*. The magnetosheath plasma bulk velocity takes similar values for the two events.

The scaling of magnetosheath turbulence is also different compared to *Event 1*. The AMPA method identifies two scaling ranges and one scale break. An extended scaling range is found for the largest scales, between 10^{-3} and roughly 0.3 Hz , where α_B takes values steeper than f^{-1} . Systematically, a power-law index close to -1.3 is found with the notable exception of the B_z component, where $\alpha \sim -1.55$. Other authors (e.g., Huang et al. 2017) have considered a spectral index of about -1.2 as pertaining to the injection regime. A complementary interpretation of this power law could be that an extended scaling range bearing properties similar to inertial-range turbulence is found for this event. The shallower power-law index might suggest that the energy cascade is slowed down by the shock and that the solar wind turbulent fluctuations are only partially destroyed while carried across the bow shock into the quasi-perpendicular magnetosheath. Indeed, an analysis of the evolution of the spectral index from the bow shock to the magnetopause for this particular event (not shown) indicates that the -1.3 index is found close to the bow shock and that it slightly steepens toward the magnetopause. This supports previous observations (Alexandrova et al. 2008; Huang et al. 2017; Teodorescu & Echim 2020) that an inertial range describing fully developed turbulence is found far from the bow shock and in the flanks of the magnetosheath. A second scaling range is found for higher frequencies, above 0.3 Hz , which exhibits values of α_B steeper than -2.2 for all magnetic components. For the evolution of the spectral index inside the magnetosheath we have divided *Event 2* into several sub-intervals and applied AMPA to each new time series.

The two magnetosheath traversals discussed here are selected from a larger collection of similar events and represent typical examples for two classes of magnetosheath turbulence with scaling behaviors pertaining to one of the two cases. A first statistical analysis of the events in this larger ensemble has not revealed the physical parameters that control the two different scaling behaviors illustrated in Figure 4. A further analysis is the subject of another study.

In a preliminary analysis of other events measured in quasi-perpendicular geometry, we have identified five other magnetosheath traversals that show findings similar to those described for *Event 1*, i.e., the solar wind turbulent properties survive the shock crossing and a narrow inertial range is found in the magnetosheath. The turbulence observed for four other magnetosheath crossings bear properties similar to *Event 2*: an extended inertial-range-like frequency domain is found at MHD scales, where the energy cascade appears to be somewhat

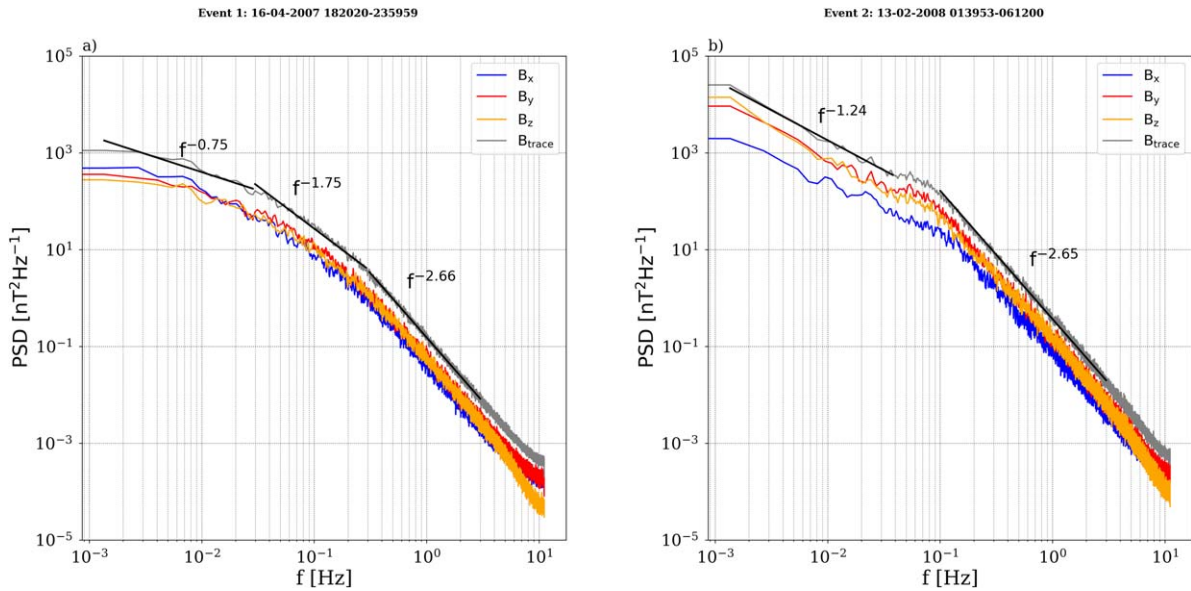


Figure 5. PSD of the GSE magnetic field components (B_x , B_y , and B_z) and the trace of the spectral matrix (B_{Tj}); solid black lines indicate the linear fits for intervals of frequencies determined with AMPA.

slowed down, and is separated by a break from another power-law regime found at kinetic scales.

The comparison of the magnetic field and plasma parameters (velocity, density, and temperature) for the two classes of events has revealed a clear difference between the bow-shock properties. For events included in the *Event 1* class, a gradual variation of all parameters is observed at the shock crossing (decrease in plasma bulk velocity, increase in density, temperature, and magnetic field), with large fluctuations and spikes of all the parameters and possibly a forward-backward movement of the shock itself. A distinct characteristic of events included in the *Event 2* class is that the shock crossing is very sharp (sudden, rapid) and all the analyzed parameters present a very abrupt transition from the solar wind into the magnetosheath. The difference between the magnetic fields measured in the vicinity of the bow shock for the two events is visible in Figure 1, where the shock crossing for *Event 1* takes place at around 16:00 and lasts for almost 30 minutes, while for *Event 2*, the transition from the solar wind into the magnetosheath environment occurs suddenly at 01:35. We have excluded the time interval between 16:10 and 18:20 from the final analysis of *Event 1* in order to obtain a stationary data set, but note that the results for the extended time series are very similar to those shown here.

5.2. Scaling of Magnetosheath Turbulence from Spectral Analysis

The scaling behavior of turbulent magnetosheath magnetic fluctuations computed with AMPA based on structure function analysis was compared with a spectral analysis applied to the same data sets of *Events 1* and 2. The results are shown in Figure 5 and illustrate spectral slopes consistent with the scaling indices derived from AMPA methodology and the second-order structure function scaling.

The PSD spectra computed for *Event 1* show three frequency regimes whose spectral slopes are close to the values of α_B derived from the structure function analysis. The spectral slopes are estimated from a linear fit over the same frequency ranges as identified with the AMPA analysis and gives the

following values for the three ranges: $\alpha = -0.75$, $\alpha = -1.75$, and $\alpha = -2.66$, respectively. Slightly steeper slopes are obtained for the sub-ion regime. Note, however, that the frequency range for the power spectrum fit is in general chosen arbitrarily, while in this case, the fitting range is determined by a consistent procedure, the AMPA method. The difference between SF versus spectral scaling in the kinetic regime could be due to the intrinsic limitation of two-point SF (discussed in the Introduction). We demonstrate that this hypothesis is true by analyzing two synthetic signals with indices steeper than -3 . We find that AMPA computes flatter spectra for both cases, as detailed in Appendix 2.

The scaling trends obtained from the AMPA analysis are also confirmed by the spectral analysis of *Event 2* data. The spectral break and the two scaling regimes are clearly visible. The similarities between the SF analysis and the spectral results are clearer for *Event 2* than for *Event 1*. Indeed, a spectral break is found at 0.1 Hz, with some differences between the magnetic field components. At the larger scales, the spectral slope is on the order of -1.24 compared with the value found by AMPA, $\alpha_B = -1.3$. At smaller scales, the spectral analysis provides a slope of about -2.65 compared to $\alpha_B = -2.4$ from AMPA. These similarities are remarkable, even more so because data from *Event 2* are most likely collected from a turbulent environment in a state far from fully developed turbulence.

6. Summary and Perspective

The scale invariance of magnetosheath turbulent fluctuations is investigated with a novel method designed to identify the power-law behavior of SF based on an idea proposed for the rank-ordered multifractal analysis by Tam & Chang (2011). The method, called the automatic multi-order power-law-fitting algorithm (AMPA), is capable of automatically determining domains of scales and frequencies where a power-law behavior is found for SF of several-moment orders as a function of scale. The method is tested on two different sets of data with a priori known statistical and spectral properties. A first set is provided by in situ magnetic field data collected in the solar wind by ACE during time periods close to the time of measurement of

the two Cluster magnetosheath crossings (Appendix 1). The statistics of the power-law exponents determined from SF analysis indicate the expected $f^{-1.66}$ scaling for the solar wind magnetic field turbulence. A second test is performed on synthetic magnetic field data with prescribed spectral slopes and spectral breaks (Appendix 2). The method correctly retrieves the scaling exponents and the respective scaling ranges.

AMPA is applied on magnetic field fluctuations measured in the Earth's magnetosheath during two Cluster crossings on 2007 April 16, 18:20:20–23:59:59 (*Event 1*), and 2008 February 13, 01:39:53–06:12:00 (*Event 2*), respectively. Both events occur for a quasi-perpendicular magnetosheath geometry. AMPA analysis shows that an inertial range can be found behind a quasi-perpendicular shock, as shown for the two events analyzed in this paper. *Event 1* displays an inertial range that spans a relatively reduced domain of scales. The second event shows an example of quasi-perpendicular conditions for which a three-decade-wide inertial range is found, and which is also characterized by a stronger anisotropy. These two events are extracted from a larger ensemble of Cluster data collected between 2007 and 2008 and represent two typical scaling behaviors observed for a relatively large number of cases. An analysis of the entire data set is the object of a future study. A comparison of AMPA results with the spectral analysis of Cluster data gives similar results. Three different power-law frequency regimes are identified in the PSD of *Event 1*, with a one-decade-long intermediate regime that shows Kolmogorov-like scaling. The PSD of *Event 2* shows only two frequency regimes with shallower scaling for the inertial regime as obtained for *Event 1*.

Previous studies suggested that solar wind turbulence is completely destroyed when crossing the quasi-perpendicular bow shock and that new fluctuations are created locally behind the shock that evolve into a developed turbulent state far from the bow shock (Huang et al. 2017). This phenomenon has been shown through spectral analysis, which indicates an energy transfer from injection scales (f^{-1}) directly to kinetic scales ($f^{-2.6}$) without the formation of an inertial range (e.g., Shevryev et al. 2006; Breuillard et al. 2018). Using a rigorous testing of power-law scaling, our study shows a remarkable similarity between scaling properties derived from structure function analysis and Fourier analysis. The two independent analyses confirm the existence of an inertial-range-like scaling in the magnetosheath behind quasi-perpendicular magnetosheath. Because the measurements are taken in the vicinity of the bow shock, this scale behavior may be a fingerprint of a possible remnant solar wind turbulence that survived the crossing of the shock. Two classes of events are observed. *Event 1* and other similar cases show a rather narrow power-law scaling above the ion characteristic scales, similar to that found in fully developed turbulence. *Event 2* and similar magnetosheath traversals distinguish themselves through what appears to be an extended inertial-range-like power-law regime, characterized by shallower spectral slopes that might be the mark of solar wind turbulence being slowed down at the bow shock and that evolves toward a fully developed state toward the magnetopause. A preliminary analysis of several events similar to the two magnetosheath traversals analyzed here seems to indicate that there is a systematic difference between the two classes of events that relates to the shock dynamics. Gradual variation over an extended period of time is

observed for the magnetic field and plasma parameters (velocity, density, and temperature) of *Event 1* while crossing the bow shock, while a sudden transition from solar wind to magnetosheath takes place for *Event 2*.

The solar wind and magnetosheath conditions differ for the two events. Slow ($\sim 300 \text{ km s}^{-1}$), less dense, and colder solar wind generates the magnetosheath of *Event 1*, and fast ($\sim 600 \text{ km s}^{-1}$), hotter, and denser solar wind produces the magnetosheath of *Event 2*. A denser magnetosheath results for *Event 1*, while the plasma bulk velocities of the two events are about 200 km s^{-1} , reflecting a larger deceleration of the solar wind during *Event 2*. The analysis of the degree of Alfvénicity, expressed in terms of normalized cross-helicity, $\sigma_c(f) = (e^+(f) - e^-(f)) / (e^+(f) + e^-(f))$ (Bruno & Carbone 2013), where $e^+(f)$ and $e^-(f)$ are the PSD of the two Elsässer variables, indicates, as expected, that the fast solar wind is more Alfvénic. The difference recorded in the solar wind between the two cases does not seem to hold in the magnetosheath, and a slightly higher degree of Alfvénicity seems to characterize *Event 1* and similar cases than that observed for *Event 2* class. Future studies will attempt to identify the physical parameters that control the occurrence of one or the other of the two types of events.

This research was supported by the European Community's Seventh Framework Programme (FP7/2007–2013) under grant agreement No. 313038/STORM; Romanian Space Agency (ROSA) via grants from the Research Program for Space Technology Development and Innovation and Advanced Research (STAR Project Nos. 122 and 182/2017); and the Romanian Ministry of Research through UEFISCDI PCCDI grant VESS (contract No. 18/2018), PN-III-P1-1.1-TE-2019-1288, and National Core Program (LAPLAS 2019). M.E. acknowledges support from the Belgian Solar Terrestrial Center of Excellence (STCE). The data analyzed in this paper and a comprehensive database specifically tailored for turbulence and nonlinear dynamics analysis is available at <http://www.storm-fp7.eu/index.php/targeted-databases>. Graphical representations of the analyzed time series and a significant part of the analysis (PSD and SF computation) can be performed with the ODYN software library (Teodorescu & Echim 2020). Online data visualization and part of the selection was done with the web-based data analysis service, AMDA (Génot et al. 2010).

Appendix

In order to validate the AMPA method, we applied it on two ensembles of data whose scaling properties are known a priori. First, we apply the technique on ACE solar wind data exhibiting clear signatures of fully developed turbulence. Second, we apply the method on synthetic data whose spectral slopes and spectral breaks are prescribed. The results are discussed below.

A.1. Statistics of the Structure Function Analysis on Solar Wind Data

We apply the AMPA technique on a collection of solar wind magnetic measurements provided by ACE in the vicinity of Earth. We compute the SF up to moment order $q=3$ for magnetic fluctuations measured during 209 slow solar wind time intervals and 128 fast solar wind samples during the

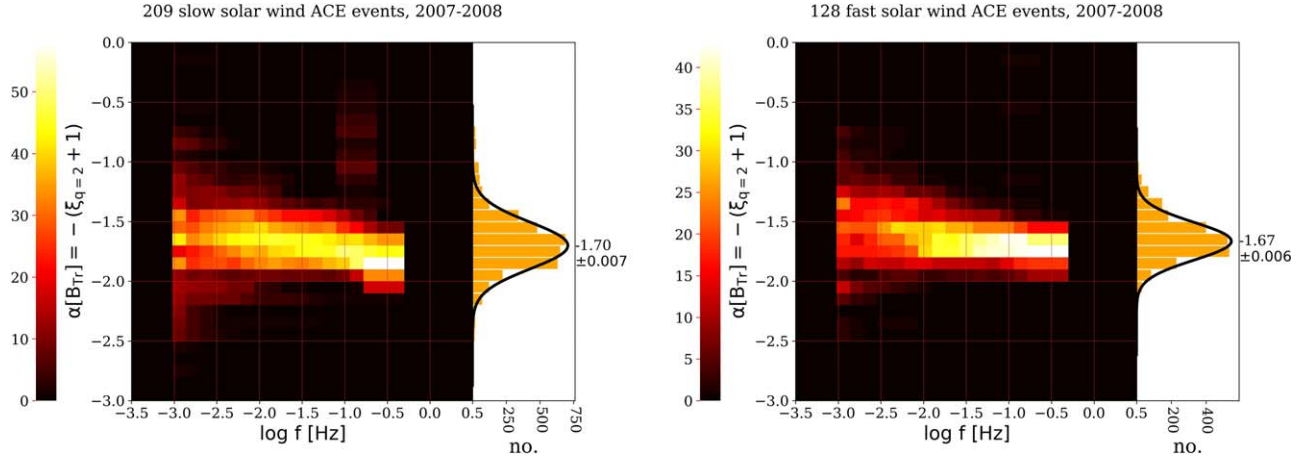


Figure 6. Two-dimensional representation of α_B , the scaling indices of solar wind magnetic fluctuations, measured by ACE and computed with AMPA. The color bar indicates the number of occurrences of the respective scaling index for the corresponding range of scales and frequencies. Left panel: scaling indices for a collection of 209 slow solar wind time series measured in 2007–2008. Right: scaling indices of a collection of 128 fast solar wind time series measured in 2007–2008.

minimum of solar cycle 24 and between 2007 and 2008. The selected solar wind data intervals correspond to the larger collection of magnetosheath traversals of the Cluster spacecraft from which *Events1* and *2* have been extracted. We compute the entire hierarchy of SF scaling exponents, ζ_q , but we further discuss results obtained for ζ_2 .

In Figure 6 we show the distribution of $\alpha_B = -(\zeta_2 + 1)$ for all solar wind data. The 2D plots show the distribution of the scaling index α_B versus the spacecraft frequency; α_B is computed for the frequency ranges determined by the AMPA algorithm; the color scale indicates the number of events with the same scaling index. The cumulative distribution shown on the Y-axis indicates that the scaling indices are normally distributed and a Gaussian fit leads to the result postulated for fully developed turbulence, $\alpha_B = -5/3$. Steeper slopes are obtained for the slow solar wind, in agreement with previous studies (see, e.g., Teodorescu et al. 2015).

A.2. Synthetic Turbulent Magnetic Fields

The method was also tested on synthetic magnetic data with prescribed spectral properties. We use the method of Roberts (2012) to generate 1D magnetic fluctuations, shown in Figure 7(a), that simulate magnetic field data measured in situ within Earth’s magnetosheath. The synthetic magnetic fields simultaneously satisfy the following constraints: (i) they are divergence free, and (ii) they have a prescribed PSD. Note that this method naturally generates discontinuities in the components of the synthetic magnetic fields.

Let us consider a fluctuating magnetic field characterized by a wavevector \mathbf{k} parallel to the x -axis and perpendicular to $\mathbf{B}(x)$. Since $\nabla \cdot \mathbf{B} = 0$, B_x must be constant; in our case, we choose $B_x = 0$. The other two components of the magnetic field are given by

$$B_i(x) = 2 \sum_{k>0} B_{ik} \sin(kx + \Phi_{ik}), \quad (\text{A1})$$

where B_{ik} and Φ_{ik} are the amplitudes and phases of the Fourier modes defining the synthetic field, while $i = y, z$. The PSD for each component of $\mathbf{B}(x)$ given by Equation (A1) is proportional to B_{ik}^2 , thus independent of the Φ_{ik} phases that are randomly distributed in the $[0, 2\pi]$ interval. We choose a magnetic field spectrum having a power-law behavior that is characterized by

three different spectral indices α_1 , α_2 , and α_3 , for three frequency intervals, ΔL_1 , ΔL_2 , and ΔL_3 , simulating the spectrum of fully developed turbulence characterized by injection, inertial, and kinetic range:

$$B_{ik}^2 \sim \begin{cases} k^{\alpha_1}, & k \leq k_{b1} \\ k^{\alpha_2}, & k_{b1} \leq k \leq k_{b2} \\ k^{\alpha_3}, & k \geq k_{b2} \end{cases} \quad (\text{A2})$$

k_{b1} is the spectral break that separates the injection range from the inertial range, while k_{b2} separates the inertial range from the dissipation range.

The synthetic magnetic field, Equation (A1), is sampled by a virtual satellite moving along the x -axis. The sampling frequency is equal to V/h , where h is the spatial resolution of the magnetic fluctuations and V is the satellite velocity in the reference frame used to generate the synthetic field. In this way, the temporal samples correspond exactly to the spatial points and provide a virtual time series of magnetic fluctuations with a prescribed power spectrum.

To test the validity of the multi-order power-law fitting approach, we generate a synthetic magnetic field as described above, using the following specific parameters: $\alpha_1 = -1$, $\alpha_2 = -1.66$, and $\alpha_3 = -2.66$, thus characterized by three power-law regimes separated by spectral breaks at prescribed wavenumbers $k_{b1} = 6.28 \times 10^{-4}$ and $k_{b2} = 3.14 \times 10^{-2}$. Considering a plasma flow velocity $V = 200 \text{ km s}^{-1}$, the two spectral breaks map at frequencies $f_1 = 0.02 \text{ Hz}$ and $f_2 = 1 \text{ Hz}$, where $f = k_b V / 2\pi$; and assuming a spatial resolution $h = 9 \text{ km}$, we obtain a temporal resolution of the virtual satellite measurements equal to 22.4 Hz, very close to the magnetometer resolution of Cluster.

The trace PSD computed for this synthetic magnetic field is shown in Figure 7(b), where the three frequency regimes and the characteristic spectral indices and frequency breaks are clearly visible. Figure 7(c) shows the logarithmic representation of the SF up to moment order $q = 3$, the linear fits and the breaks between adjacent scale regimes determined with AMPA. The inset plot shows the 2D representation of the second-order SF scaling indices and the positions of the spectral breaks. It is seen that the computed values of the power-law exponents and the breaks are very close to the prescribed values, which is a

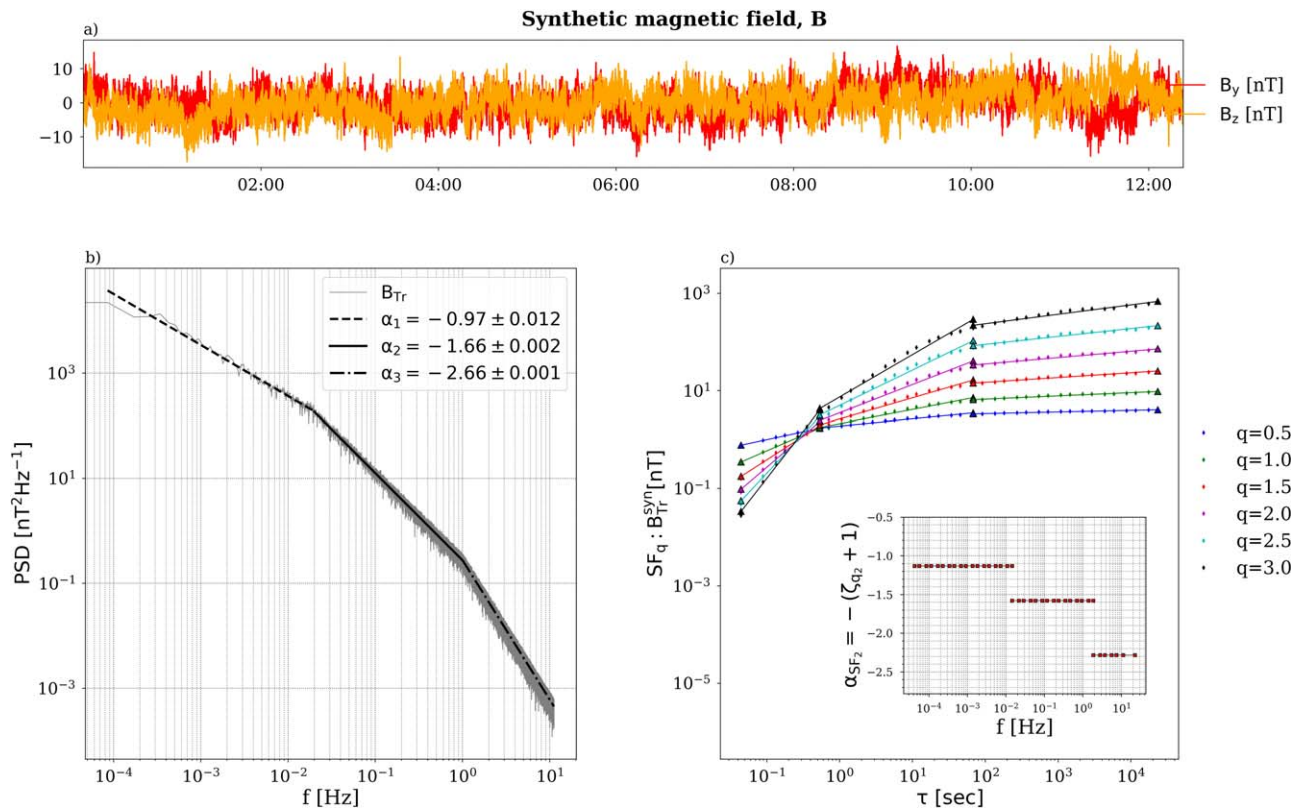


Figure 7. (a) Time series of the synthetic magnetic field, B_{syn} . (b) PSD of B_{syn} showing three distinct power-law frequency regimes and two spectral breaks. (c) Structure function scaling indices determined for B_{syn} using the AMPA approach.

good indication that the algorithm is able to accurately determine these parameters.

A shallower index is obtained with AMPA at sub-ion scales, ~ -2.3 . To test whether the difference from the expected index (-2.66) is a consequence of the limitations of the two-point second-order SF (described in the Introduction), we have applied AMPA on two synthetic signals with steeper indices in the kinetic regime, i.e., -3.66 and -5 . As expected, we found that an index close to -2.6 is computed by AMPA in both cases, indicating that indeed, the difference we observe between scalings determined from PSD and AMPA is strongly related to how fluctuations are estimated.

ORCID iDs

Eliza Teodorescu <https://orcid.org/0000-0002-5294-0075>

Marius Echim <https://orcid.org/0000-0001-7038-9494>

Gabriel Voitcu <https://orcid.org/0000-0002-9474-7468>

References

- Alexandrova, O., Chen, C. H. K., Sorriso-Valvo, L., Horbury, T. S., & Bale, S. D. 2013, *SSRv*, 178, 10
- Alexandrova, O., Lacombe, C., & Mangeney, A. 2008, *AnGeo*, 26, 3585
- Alexandrova, O., Lacombe, C., Mangeney, A., Grappin, R., & Maksimovic, M. 2012, *ApJ*, 760, 121
- Alexandrova, O., Saur, J., Lacombe, C., et al. 2009, *PhRvL*, 103, 16
- Anselmet, F., Gagne, Y., Hopfinger, E. J., & Antonia, R. A. 1984, *JFM*, 140, 63
- Bale, S. D., Kasper, J. C., Howes, G. G., et al. 2009, *PhRvL*, 103, 211101
- Balogh, A., Dunlop, M. W., Cowley, S. W. H., et al. 1997, *SSRv*, 79, 65
- Balogh, A., Schwartz, S. J., Bale, S. D., et al. 2005, in *Outer Magnetospheric Boundaries: Cluster Results*, ed. G. Paschmann et al. (Dordrecht: Springer)
- Benzi, R., Ciliberto, S., Tripiccone, R., et al. 1993, *PhRvE*, 48, 29
- Boldyrev, S., & Perez, J. C. 2012, *ApJL*, 758, L44

- Breuillard, H., Matteini, L., Argall, M. R., et al. 2018, *ApJ*, 859, 127
- Bruno, R. 2019, *E&SS*, 6, 656
- Bruno, R., Bavassano, B., & Villante, U. 1985, *JGR*, 90, 4373
- Bruno, R., & Carbone, V. 2013, *LRSP*, 2, 4
- Bruno, R., Telloni, D., Sorriso-Valvo, L., et al. 2019, *A&A*, 627, A96
- Burlaga, L. F. 1991, *JGR*, 96, 5847
- Cairns, I. H., Fairfield, D. H., Anderson, R. R., et al. 1995, *JGR*, 100, 47
- Carbone, V. 1994, *AnGeo*, 12, 585
- Chang, T. 2015, *An Introduction to Space Plasma Complexity* (Cambridge: Cambridge Univ. Press)
- Chen, C. H. K., & Boldyrev, S. 2017, *ApJ*, 842, 122
- Chen, C. H. K., Boldyrev, S., Xia, Q., & Perez, J. C. 2013, *PhRvL*, 110, 259901
- Chen, C. H. K., Horbury, T. S., Schekochihin, A. A., et al. 2010, *PhRvL*, 104, 255002
- Chen, C. H. K., Salem, C. S., Bonnell, J. W., Mozer, F. S., & Bale, S. D. 2012, *PhRvL*, 109, 035001
- Chen, S., Doolen, G. D., Kraichnan, R. H., & She, Z. 1993, *PhFIA*, 5, 458
- Czaykowska, A., Bauer, T. M., Treumann, R. A., & Baumjohann, W. 2001, *AnGeo*, 19, 275
- Dudok de Wit, T. 2004, *PhRvE*, 70, 055302
- Dudok de Wit, T., Alexandrova, O., Furno, I., Sorriso-Valvo, L., & Zimbardo, G. 2013, *SSRv*, 178, 665
- Dudok de Wit, T., & Krasnosel'skikh, V. V. 1996, *Processes Geophys*, 3, 262
- Dwivedi, N. K., Kumar, S., Kovacs, P., et al. 2019, *Ap&SS*, 364, 101
- Eastwood, J. P., Lucek, E. A., Mazelle, C., et al. 2005, *SSRv*, 118, 41
- Escoubet, C. P., Schmidt, R., & Goldstein, M. L. 1997, *SSRv*, 79, 11
- Farris, M. H., Petrinec, S. M., & Russell, C. T. 1991, *GeoRL*, 18, 1821
- Farris, M. H., & Russell, C. T. 1994, *JGRA*, 99, 17681
- Frisch, U. 1995, *Turbulence: The legacy of A.N. Kolmogorov* (Cambridge, New York: Cambridge Univ. Press)
- Frisch, U., Pierre-Louis, S., & Mark, N. 1978, *JFM*, 87, 719
- Génot, V., Jacquey, C., M. Bouchemir, M., et al. 2010, *AdSpR*, 45, 9
- Goldstein, B. E., Smith, E. J., Balogh, A., et al. 1995, *GeoRL*, 22, 3393
- Grappin, R., Mangeney, A., & Marsch, E. 1989, in *Turbulence and Nonlinear Dynamics in MHD Flows*, ed. M. Meneguzzi, A. Pouquet, & P. L. Sulem (Amsterdam: North-Holland), 81
- Grappin, R., Mangeney, A., & Marsch, E. 1990, *JGR*, 95, 8197
- Grauer, R., Krug, J., & Marliani, C. 1994, *PhLA*, 195, 335

- Grošelj, D., Chen, C. H. K., Mallet, A., et al. 2019, *PhRvX*, **9**, 031037
- Horbury, T. S., & Balogh, A. 1997, *NPGeo*, **4**, 185
- Horbury, T. S., Balogh, A., Forsyth, R. J., & Smith, E. J. 1996, *JGRA*, **101**, 405
- Howes, G. G., TenBarge, J. M., Dorland, W., et al. 2011, *PhRvL*, **107**, 035004
- Huang, S. Y., Hadid, L. Z., Sahraoui, F., Yuan, Z. G., & Deng, X. H. 2017, *ApJL*, **836**, L10
- Huang, S. Y., Sahraoui, F., Deng, X. H., et al. 2014, *ApJL*, **789**, L28
- Huang, Y., Lu, Z., & Schmitt, F. 2010, *PhRvE*, **82**, 026319
- Iroshnikov, P. S. 1964, *SvA*, **7**, 566
- Jerab, M., Nemecek, Z., Safrankova, J., Jelinek, K., & Merka, J. 2005, *P&SS*, **53**, 85
- Kiyani, K., Chapman, S. C., & Hnat, B. 2006, *PhRvE*, **74**, 051122
- Kiyani, K. H., Chapman, S. C., Khotyaintsev, Yu. V., Dunlop, M. W., & Sahraoui, F. 2009, *PhRvL*, **103**, 075006
- Klein, K. G., Howes, G. G., & Tenbarger, J. M. 2014, *ApJL*, **790**, L20
- Kolmogorov, A. N. 1941, *DoSSR*, **30**, 301
- Kolmogorov, A. N. 1962, A Refinement of Previous Hypotheses Concerning the Local Structure of Turbulence in a Viscous Incompressible Fluid at High Reynolds Number, Vol. 13 (Cambridge: Cambridge Univ. Press), 82
- Kraichnan, R. H. 1965, *PhFl*, **8**, 1385
- Lesur, M., Diamond, P. H., & Kosuga, Y. 2014a, *PhPl*, **21**, 112307
- Lesur, M., Diamond, P. H., & Kosuga, Y. 2014b, *PPCF*, **56**, 075005
- Lin, R. L., Zhang, X. X., Liu, S. Q., Wang, Y. L., & Gong, J. C. 2010, *JGR*, **115**, A04207
- Lohse, D., & Müller-Groeling, A. 1995, *PhRvL*, **74**, 1747
- Lohse, D., & Müller-Groeling, A. 1996, *PhRvE*, **54**, 395
- Mailyan, B., Munteanu, C., & Haaland, S. 2008, *AnGeo*, **26**, 2383
- Marsch, E., & Tu, C.-Y. 1990, *JGR*, **95**, 11945
- Matthaeus, W. H., & Goldstein, M. L. 1982, *JGR*, **87**, 10347
- Meneveau, C., & Sreenivasan, K. R. 1987a, *NuPhB*, **2**, 49
- Meneveau, C., & Sreenivasan, K. R. 1987b, *PhRvL*, **59**, 1424
- Monin, A. S., & Yaglom, A. M. 1975, in *Statistical Fluid Mechanics: Mechanics of Turbulence*, ed. J. Lumley (Cambridge, MA: MIT Press), c1971
- Munteanu, C., Haaland, S., Mailyan, B., Echim, M., & Mursula, K. 2013, *JGRA*, **118**, 3985
- Newell, A. C., Nazarenko, S., & Biven, L. 2001, *PhyD*, **152**, 520
- Omidi, N., Blanco-Cano, X., & Russell, C. T. 2005, *JGR*, **110**, A12212
- Omidi, N., Sibeck, D., Gutynska, O., & Trattner, K. J. 2014, *JGRA*, **119**, 2593
- Pagel, & Balogh, A. 2001, *NPGeo*, **8**, 313
- Paladin, G., & Vulpiani, A. 1987, *PhR*, **156**, 147
- Perri, S., Servidio, S., Vaivads, A., & Valentini, F. 2017, *ApJS*, **231**, 4
- Pucci, F., Matthaeus, W. H., Chasapis, A., et al. 2018, *ApJ*, **867**, 10
- Pulkkinen, A., Klimas, A., Vassiliadis, D., Uritsky, V., & Tanskanen, E. 2006, *JGR*, **111**, A03305
- Rème, H., Cottin, F., Cros, A., et al. 1997, *SSRv*, **79**, 303
- Roberts, D. A. 2012, *PhRvL*, **109**, 231102
- Roberts, D. A., Goldstein, M. L., Klein, L. W., & Matthaeus, W. H. 1987a, *JGR*, **92**, 11021
- Roberts, D. A., Goldstein, M. L., Klein, L. W., & Matthaeus, W. H. 1987b, *JGR*, **92**, 12023
- Roberts, O. W., Li, X., & Li, B. 2013, *ApJ*, **769**, 58
- Roberts, O. W., Nakamura, R., Torkar, K., et al. 2020a, *ApJS*, **250**, 2
- Roberts, O. W., Verscharen, D., Narita, Y., et al. 2020b, *PhRvR*, **2**, 043253
- Russell, C. T., & Farris, M. H. 1995, *AdSpR*, **15**, 285
- Ruzmaikin, A. A., Feynman, J., Goldstein, B. E., Smith, E. J., & Balogh, A. 1995, *JGRD*, **100**, 3395
- Sahraoui, F., Belmont, G., Rezeau, L., et al. 2006, *PhRvL*, **96**, 075002
- Sahraoui, F., Goldstein, M. L., Robert, P., & Khotyaintsev, Yu. V. 2009, *PhRvL*, **102**, 231102
- Sahraoui, F., Huang, S. Y., Belmont, G., et al. 2013, *ApJ*, **777**, 1
- Salem, C. S., Howes, G. G., Sundkvist, D., et al. 2012, *ApJL*, **745**, L9
- Schulz-DuBois, E. O., & Rehberg, I. 1981, *ApPhy*, **24**, 323
- Schwartz, S. J., Burgess, D., & Moses, J. J. 1996, *AnGeo*, **14**, 1134
- She, Z.-S., & Leveque, E. 1994, *PhRvL*, **72**, 3
- Shevryev, N. N., Zastenker, G. N., Eigens, P. E., & Richardson, J. D. 2006, *AdSpR*, **37**, 1516
- Shue, J.-H., Song, P., Russell, C. T., et al. 1998, *JGRA*, **103**, 17691
- Smith, C., L'Heureux, J., Ness, N., et al. 1998, *SSRv*, **86**, 613
- Smith, C. W., Hamilton, K., Vasquez, B. J., & Leamon, R. J. 2006, *ApJL*, **645**, L1
- Stolovitzky, G., Kailasnath, P., & Sreenivasan, K. R. 1992, *PhRvL*, **69**, 1178
- Stone, E. C., Frandsen, A. M., Mewaldt, R. A., et al. 1998, *SSRv*, **86**, 1
- Sundkvist, D., Retino, A., Vaivads, A., & Bale, S. D. 2007, *PhRvL*, **99**, 025004
- Tam, S. W. Y., & Chang, T. T. 2011, *Processes Geophys*, **18**, 405
- Tátrallyay, M., Erdős, G., Németh, Z., Verigin, M. I., & Vennerstrom, S. 2012, *AnGeo*, **30**, 1675
- Taylor, G. I. 1938, *RSPSA*, **164**, 476
- Telloni, D. 2021, *Atmos*, **12**, 44
- Telloni, D., Carbone, F., Bruno, R., et al. 2019, *ApJ*, **887**, 160
- Teodorescu, E., Echim, M., Munteanu, C., et al. 2015, *ApJL*, **804**, L41
- Teodorescu, E., & Echim, M. M. 2020, *E&SS*, **7**, e2019EA001004
- Thoroddsen, S. T., & Van Atta, C. W. 1992, *PhFl*, **A4**, 2592
- Tsurutani, B., & Stone, R. (ed.) 1985, *Geophysical Monograph Series*, 30 (Washington, DC: AGU)
- Tu, C. Y., & Marsch, E. 1995, *SSRv*, **73**, 1
- Tu, C.-Y., Roberts, D. A., & Goldstein, M. L. 1989, *JGR*, **94**, 13575
- Valentini, F., Servidio, S., Perrone, D., et al. 2014, *PhPl*, **21**, 082307
- Verigin, M., Kotova, G., Szabo, A., et al. 2001a, *EP&S*, **53**, 1001
- Verigin, M., Slavin, J., Szabo, A., Kotova, G., & Gombosi, T. 2003, *EP&S*, **55**, 33
- Verigin, M. I., Kotova, G. A., Bezrukh, V. V., Zastenker, G. N., & Nikolaeva, N. 2009, *Ge&Ae*, **49**, 1176
- Verigin, M. I., Kotova, G. A., Slavin, J., et al. 2001b, *AdSpR*, **28**, 857
- Vincent, A., & Meneguzzi, M. 1991, *JFM*, **225**, 1
- Voros, Z., Yordanova, E., Echim, M. M., Consolini, G., & Narita, Y. 2016, *ApJL*, **819**, L15
- Wang, T., He, J., Alexandrova, O., Dunlop, M., & Perrone, D. 2020, *ApJ*, **898**, 91